Supplementary Materials: Non-collinear and asymmetric polar moments at back-gated $SrTiO_3$ interfaces

Fryderyk Lyzwa[1], Yurii G. Pashkevich[2], Premysl Marsik[1], Andrei Sirenko[3], Andrew Chan[4], Benjamin P.P. Mallett[4,5], Meghdad Yazdi-Rizi[1], Bing Xu[1], Luis M. Vicente-Arche[6], Diogo C. Vaz[6], Gervasi Herranz[7], Maximilien Cazayous[8], Pierre Hemme[8], Katrin Fürsich[9], Matteo Minola[9], Bernhard Keimer[9], Manuel Bibes[6], and Christian Bernhard[1]

[1]*Department of Physics and Fribourg Center for Nanomaterials, University of Fribourg, Chemin du Musée 3, CH-1700 Fribourg, Switzerland*
[2]*O. O. Galkin Donetsk Institute for Physics and Engineering NAS of Ukraine, UA-03028 Kyiv, Ukraine*
[3]*Department of Physics, New Jersey Institute of Technology, Newark, New Jersey 07102, USA*
[4]*School of Chemical Sciences and the MacDiarmid Institute for Advanced Materials and Nanotechnology, The University of Auckland, Auckland, New Zealand*
[5]*Robinson Research Institute, Victoria University of Wellington, 69 Gracefield Rd., Lower Hutt 5010, New Zealand*
[6]*Unité Mixte de Physique, CNRS, Thales, Université Paris-Saclay, 91767 Palaiseau, France*
[7]*Institut de Ciència de Materials de Barcelona (ICMAB-CSIC), Campus UAB, 08193 Bellaterra, Catalonia, Spain*
[8]*Laboratoire Matériaux et Phénomènes Quantiques (UMR 7162 CNRS), Université de Paris, 75205 Paris Cedex 13, France*
[9]*Max-Planck-Institut für Festkörperforschung, Heisenbergstrasse 1, 70569 Stuttgart, Germany*

Correspondence should be addressed to Fryderyk Lyzwa (fryderyk.lyzwa@unifr.ch) or Christian Bernhard (christian.bernhard@unifr.ch)

Contents

Supplementary Note 1: Sample growth and transport properties

$LaAlO_3/SrTiO_3(001)$ samples: LAO deposition was carried out by pulsed laser deposition onto TiO_2-terminated (001) oriented STO substrates. The LAO was ablated from a crystalline LAO target, with a target-substrate distance of ~5.5 cm, by a KrF laser (λ = 248 nm) with a repetition rate of 1 Hz and laser fluence of 1 J/cm^2. We used reflection high-energy electron diffraction (RHEED) during growth to monitor the layer-by-layer growth and stop the growth after 5 unit cells. After the LAO deposition, the sample was cooled to T = 550 °C at a pressure of p_{O2} = 0.1 mbar. Once at T = 550 °C, the sample was annealed p_{O2} = 200 mbar for one hour. Finally, the sample was brought to room temperature by passive cooling at p_{O2} = 200 mbar.

$AlO_x/SrTiO_3(001)$ and $AlO_x/KTaO_3(001)$ samples: Al films were deposited at room temperature by dc magnetron sputtering on non-terminated (001)-oriented STO and KTO substrates under an Ar partial pressure of 4.5×10^{-4} mbar and a substrate-to-target distance of 7 cm. The deposition rates of the Al layer was 0.1 nm/s, under an operating dc current of 30 mA. The Al thickness was 1.8 nm.

Transport properties characterization: The samples were measured using a PPMS DynaCool system from Quantum Design after bonding with Al wires in van der Pauw configuration. Supplementary Fig. 1 shows the R_s vs T plots and the transverse resistance (R_{xy}) as a function of magnetic field, applied perpendicular to the film. The non-linear Hall trace ($R_{xy}(H)$) can be attributed to a multi-band regime, where two types of carriers in lighter d_{xy} and heavier $d_{xz,yz}$ bands contribute to conduction. 2DEGs carrier density and mobilities are estimated considering the two-band Drude model, according to which:

$$R_s(0) = \frac{1}{e}\left(\frac{1}{n_1\mu_1 + n_2\mu_2}\right) \tag{S1}$$

$$R_{xy}(H) = -\frac{H}{e}\frac{(n_1{\mu_1}^2 + n_2{\mu_2}^2) + (n_1 + n_2)(\mu_1\mu_2 H)^2}{(n_1\mu_1 + n_2\mu_2)^2 + (n_1 + n_2)^2(\mu_1\mu_2 H)^2} \tag{S2}$$

The values obtained after applying the aforementioned constraints during the fitting are shown in Supplementary Table 1.

	$n_1(cm^{-2})$	$n_2(cm^{-2})$	$\mu_1(cm^2/V\cdot s)$	$\mu_2\ (cm^2/V\cdot s)$
LAO/STO	1.7×10^{13}	8.8×10^{12}	574	1562
AlO_x/STO	5.1×10^{13}	2.3×10^{12}	193	1175
AlO_x/KTO	4.1×10^{13}	2.2×10^{10}	44	1400

Supplementary Table 1: Carrier properties of the $LaAlO_3/SrTiO_3$, $AlO_x/SrTiO_3$ and $AlO_x/KTaO_3$ samples.

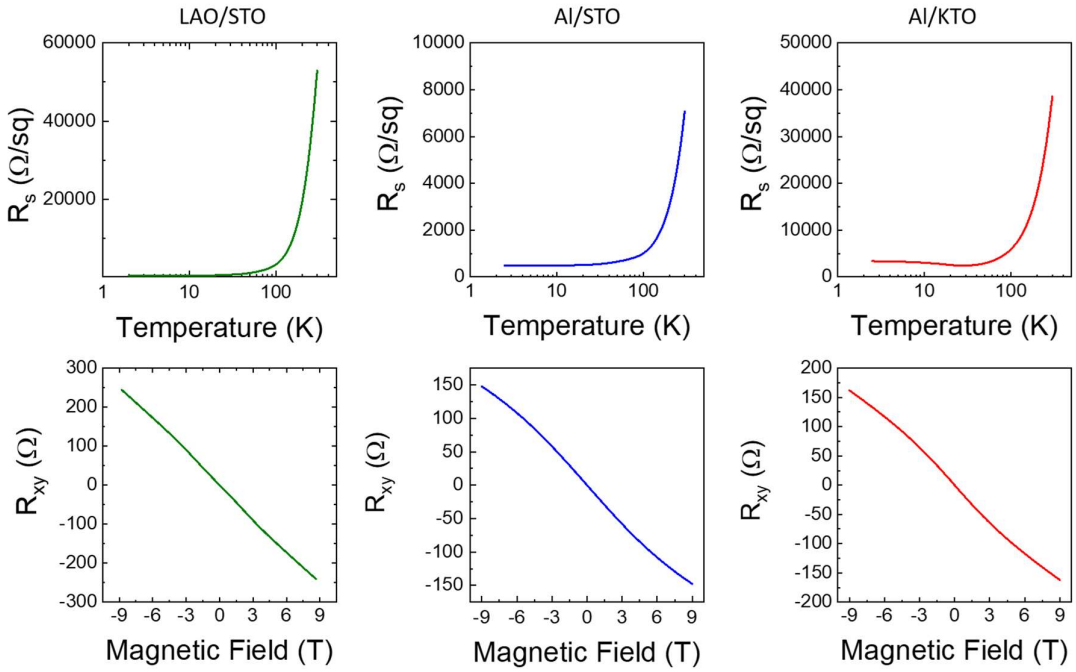

Supplementary Figure 1: Magneto-transport properties of $LaAlO_3/SrTiO_3$, $AlO_x/SrTiO_3$ and $AlO_x/KTaO_3$. *The total carrier densities (n_1+n_2) are estimated to be 2.6×10^{13} cm^{-2}, 5.3×10^{13} cm^{-2} and 4.1×10^{13} cm^{-2}, respectively.*

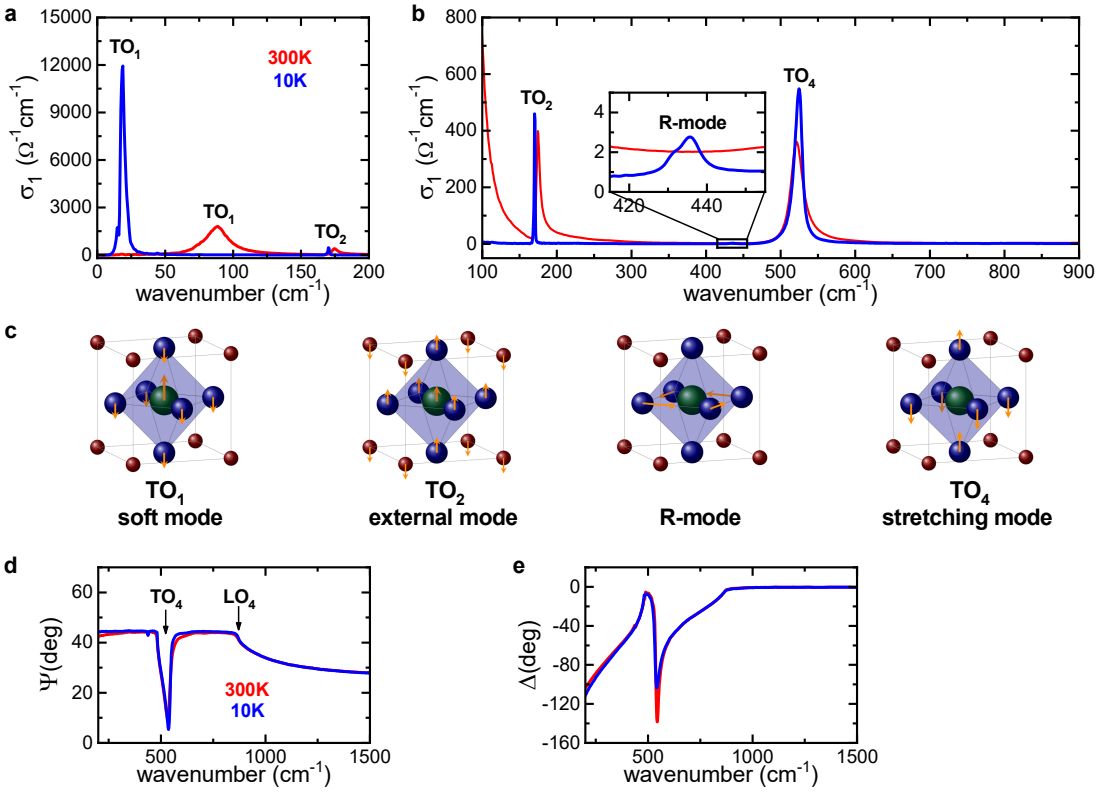

Supplementary Figure 2: Infrared response of bulk $SrTiO_3$. *Infrared-active longitudinal-optical (LO) and transverse-optical (TO) phonon modes of $SrTiO_3$. The data have been obtained via a combination of normal incidence reflectivity and spectroscopic ellipsometry (at an incidence angle of 80 degrees). (a,b) Spectra of the real part of the optical conductivity σ_1 of $SrTiO_3$ at 300 K (red curve) and 10 K (blue curve), which are governed by four infrared-active phonon modes. The soft mode (TO_1, shown in (a)), softens and increases drastically in strength when cooling from 300 to 10 K. The R-mode in (b) originates from the antiphase rotation of the neighbouring oxygen octahedra. It develops only in the tetragonal state and thus below the so-called antiferrodistortive (AFD) transition at $T^* \approx 105$ K. (c) Schematics of the atomic vibrations for the corresponding phonon mode (adapted from [1]). Note that the TO_3 mode is silent and therefore does not appear in the infrared spectra [2]. (d), (e) Spectra of the ellipsometric angles Ψ and Δ showing the TO_4 mode and the corresponding LO_4 edge at which the real part of the dielectric function crosses zero.*

Supplementary Note 2: Ellipsometry technique for anisotropic samples

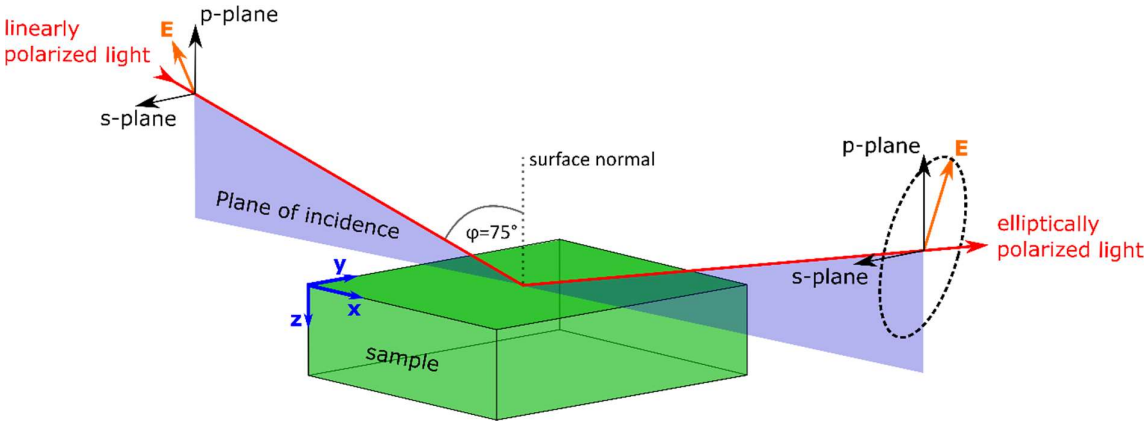

Supplementary Figure 3: Ellipsometry measurement principle. *Shown is the orientation of the sample and its surface with respect to the plane of incidence that is defined by the wave vectors of the incoming and the reflected light.*

The ellipsometric response of anisotropic samples depends on the orientation of the sample and its surface with respect to the plane of incidence of the photons, (see Supplementary Figure 3). The so-called pseudo-dielectric function <ε> is derived from the measured ellipsometric angles Δ, Ψ according to:

$$\rho = \tan\Psi * e^{i\Delta} \tag{S3}$$

$$< \varepsilon >= \sin^2(\varphi) * \left[1 + \tan^2(\varphi) * \left(\frac{1+\rho}{1-\rho}\right)\right] \tag{S4}$$

with φ being the angle of incidence and ρ the complex reflectivity ratio of the p- and s-polarized light [3]. For an anisotropic material that can be described with an orthogonal set of unit vectors, the obtained pseudo-dielectric function <ε> is usually governed by the x-component of the dielectric function [4], with the x-axis defined by the cross-section of the plane of incidence of the photons with the sample surface, see Supplementary Figure 3. Exceptions occur close to the energy of an LO mode in the out-of-plane component (z-component) of the dielectric function at which the real part undergoes a zero crossing. As outlined e.g. in Refs. [5], [4], in the vicinity of such a LO mode the ellipsometry data can be rather sensitive to the z-component of the dielectric function. Here the strength of the z-axis response is roughly proportional to the so-called loss-function, $Im\left\{-\frac{1}{\varepsilon_z}\right\} = \frac{\varepsilon_{2,z}}{\varepsilon_{1,z}^2+\varepsilon_{2,z}^2}$, which becomes sizeable if ε_2 is small. This is the case in the vicinity of the LO_4 edge of STO for which the TO modes are at lower frequency and sufficiently narrow and there is also no Drude-response (except for a very weak one from the 2DEG). As shown in Fig. 1e of the manuscript and in Supplementary Note 6, the analysis of the LO_4 edge anomaly in the ellipsometry data thus provides additional information about the z-axis components of the underlying polar moment.

Supplementary Note 3: Origin of the infrared-active R-mode (at 438 cm^{-1}) in the tetragonal phase

$SrTiO_3$ undergoes a structural phase transition at $T^* \approx 105$ K from a cubic high temperature phase (space group P*m*-3*m*, one formula unit per cell) to a tetragonal phase at low temperature with a doubled unit cell (as compared to the cubic one) along the C_4 – tetragonal axis (space group I4/*mcm*, two formula units per cell). This unit cell doubling in the tetragonal state arises from the freezing of an antiferrodistortive (AFD) mode from the R-point of the cubic Brillouin zone (BZ) which involves an out-of-phase rotation of the corner shared oxygen octahedra along the C_4-axis with a rotation angle of about $\theta_z \approx 2.5°$.

The enlarged unit cell in the AFD state of $SrTiO_3$ gives rise to several new phonon modes at the Γ-point that are backfolded from the R-point of the cubic BZ. The distribution of the phonon modes among the irreducible representations of the I4/*mcm* group with the C_4-axis chosen along the z-axis is as follows:

$$1A_{1g} + 1A_{1u} + 2A_{2g} + 4A_{2u}(z) + 1B_{1g} + 1B_{1u} + 2B_{2g} + (2+4)E_u(x,y) + (1+2)E_g \qquad \text{(S5)}$$

One of the $A_{2u}(z)$ and two of the $E_u(x,y)$ modes are of acoustic origin. The phonon modes from the R-point of the cubic BZ are denoted in red and are assigned according to the analysis of their normal coordinates. In particular, there exist two E_u optical polar modes from the R-point of the cubic BZ. The Ti ions in the 4c Wyckoff positions Ti1 - (0,0,0) and Ti2-(0,0,1/2) participate in these E_u-polar modes with the following normal coordinates:

$$E_u \quad \begin{cases} -l_y = -u_{1y}(Ti) + u_{2y}(Ti) \\ l_x = u_{1x}(Ti) - u_{2x}(Ti) \end{cases}; \quad \begin{cases} p_x = u_{1x}(Ti) + u_{2x}(Ti) \\ p_y = u_{1y}(Ti) + u_{2y}(Ti) \end{cases}; \qquad \text{(S6)}$$

where $u_{\alpha i}$ denotes the displacement of the titanium ion α along the cartesian direction i. The normal coordinates l_i and p_i transform as the basic functions of the E_u irreducible representation. The first column describes the vibrations of a nonpolar antiferroelectric mode at the R-point of the cubic BZ whereas the second column accounts for the polar vibrations. In the tetragonal phase, due to presence of the AFD distortions, the two types of normal coordinates get mixed and the dynamic phonon matrix contains the additional term:

$$\ldots + M(\theta_z)(l_x p_y - l_y p_x) + \ldots \qquad \text{(S7)}$$

Due to this mixing term, the doubly degenerate, antiferroelectric R-mode (which consists of mainly titanium antiferroelectric *l* - type vibrations and would otherwise be non-polar) becomes infrared active, as was theoretically described in Ref. [6].

The dynamic matrix constant *M*, which determines the admixture of the dynamical polar moment $p_{x,y}$ to the antiferroelectric vibrations $l_{y,x}$, is proportional to the AFD order parameter $\theta_z \approx 2.5°$ and thus rather small. Accordingly, the infrared-active R-mode has a much lower oscillator strength than the other polar TO modes, in good agreement with experiment (see Supplementary Figure 2b). A sketch of the ionic vibration pattern of the weakly infrared-active R-mode is displayed in Supplementary Figure 4.

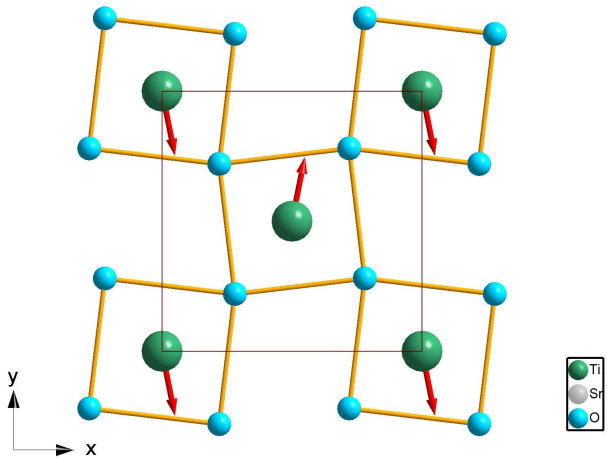

Supplementary Figure 4: Ionic vibration pattern of the infrared-active R-mode. *This sketch demonstrates the l_y, p_x pattern of the displacements of the titanium ions in the polar R-mode at 438 cm^{-1} in the antiferrodistortive nonpolar phase. Shown is the ab-plane cut of the crystallographic cell of the I4/mcm space group. The degenerate mode with the corresponding l_x, p_y displacements is obtained by 90° rotation of all arrows around the z-axis.*

Supplementary Note 4: Origin of the splitting of the R-mode (438 cm^{-1}) in the ferroelectric state or in the presence of an otherwise induced static polar moment

The interaction which accounts for the splitting of the R-mode, with a strong redshift of the component for which the polarization is parallel to the static polar moment, arises from the mixing term in eq. S7. It describes an antiferroelectric-ferroelectric (AFFE) coupling that is analogous to the Dzyaloshinsky-Moriya-type coupling in magnets which leads to a canted antiferromagnetic order with a net ferromagnetic moment whose magnitude is proportional to the canting angle. In the case of $SrTiO_3$, this AFFE-coupling term originates from the anharmonic coupling between the AFD, AFE and FE modes of the cubic phase [6]. The freezing of the AFD mode in the tetragonal phase gives rise to a bilinear interaction in the form of eq. S7.

Note that in accordance with Landau theory, in the presence of the AFFE bilinear term in the free energy, the transition in a polar phase with a static polar moment P_x will be accompanied by the formation of an antiferroelectric static moment L_y. Accordingly, in $SrTiO_3$ the polar phase is canted with a canting angle that is proportional to the value of the AFFE-coupling constant.

In the following, we discuss a toy model which captures the basic concept of the redshift phenomenon of the R-mode (E_u(x,y)–mode, with frequency Ω_{0R}). For simplicity, we consider solely the displacements of the titanium ions, $l_{x,y}$, $p_{x,y}$ in (S4) without contributions from the other ions. The respective energy of the R-mode has the following form:

$$\ldots\frac{\dot{l}_x^2+\dot{l}_y^2}{2}+\frac{\dot{p}_x^2+\dot{p}_y^2}{2}+\frac{k_{LX}l_x^2+k_{LY}l_y^2}{2}+\frac{k_{PX}p_x^2+k_{PY}p_y^2}{2}+M(\theta_z)(l_xp_y-l_yp_x)+\ldots \qquad \text{(S8)}$$

Here $k_{LX,Y}$ and $k_{PX,Y}$ are the stiffness parameters for the respective displacements. All constants are normalized according to the reduced mass of the Ti ions.

The system of the equations of motion consists of two independent blocks containing $\{l_x,p_y\}$ and $\{l_y,p_x\}$ displacements which yield the same energy of the R-mode $\Omega_R(x) = \Omega_R(y) = \Omega_{0R}$ for x- and y-polarizations if $k_{PX} = k_{PY} = k_P$ and $k_{LX} = k_{LY} = k_L$

$$\Omega_R^2(x) = \frac{1}{2}[k_{LY} + k_{PX} + \sqrt{(k_{LY} - k_{PX})^2 + 4M^2}]$$
$$\Omega_R^2(y) = \frac{1}{2}[k_{LX} + k_{PY} + \sqrt{(k_{LX} - k_{PY})^2 + 4M^2}] \quad \text{(S9)}$$

In the absence of the AFFE interaction we have $\Omega^2_{0R} \approx k_L$. Using results of the DFT calculations for displacement patterns of the R-mode in the AFD phase $\{l_x = 0.995; p_y = -0.077\}$ [6] one can roughly estimate the value of the AFFE coupling constant $M \approx -0.054\ \Omega^2_{0R}$. Here we suppose that $k_L > k_P$.

Respectively, the value of the antiferroelectric order parameter L_y in the polar phase with the static polar moment P_x of titanium ions can be routinely derived from the Landau theory of phase transitions:

$$L_y = -\frac{M}{k_L} P_x = 0.057 P_x \quad \text{(S10)}$$

The appearance of the two kind of order parameters P_x and L_y in the polar phase of $SrTiO_3$ implies that the corresponding stiffness parameters k_{PX} and k_{LY} are both softened such that $k_{PX} = k_{PS} < k_P$ and $k_{LY} = k_{LS} < k_L$ and subsequently $\Omega_R(x) < \Omega_R(y)$. This highlights our central point that a polar distortion with a static moment **P** gives rise to an anisotropy in the frequency of the R-mode with a pronounced redshift of the component that is parallel to **P**. A corresponding effect is expected if the polar moment and the accompanying antiferroelectric moment are induced by an external electric field which is the case in bulk $SrTiO_3$ at temperature below 40 K and electric fields in excess of 2 to 5 kV/cm [7].

An additional source of the R-mode splitting in the polar phase arises after accounting for the *R*-mode specific anharmonic interactions in the form:

$$.... + \frac{G}{2}[p_x^2 l_y^2 + p_y^2 l_x^2] + \frac{H}{2}[p_x^2 l_x^2 + p_y^2 l_y^2] + ... \quad \text{(S11)}$$

Note that the anharmonicity constants G and H do not depend on the small AFD order parameter, as they exist already in the cubic phase of $SrTiO_3$. Following the model of linearly coupled anharmonic oscillators which was successfully applied to $SrTiO_3$ [8], [9] one obtains a renormalization of the stiffness constants in equation (S9). Particularly, in the P_x and L_y polar phase the new stiffness constants have the form:

$$\tilde{k}_{LY} = k_{LY} + G < p_x^2 >= k_{LY} + GP_x^2; \quad \tilde{k}_{PX} = k_{PX} + G < l_y^2 >= k_{PX} + GL_y^2;$$
$$\tilde{k}_{LX} = k_{LX} + H < p_x^2 >= k_{LX} + HP_x^2; \quad \tilde{k}_{PY} = k_{PY} + H < l_y^2 >= k_{PY} + HL_y^2; \quad \text{(S12)}$$

The renormalization of the polar stiffness constants $k_{PX,Y}$ can be neglected as they contain the small parameter $(L_y)^2$.

The magnitude of the constant H is expected to be very small. This is also confirmed by our experimental data which show that the R-mode is hardly affected (neither shifted nor split) by the application of a positive voltage (see Fig. 1a,c in the manuscript). Specifically, we consider the case of an AFD domain for which the C_4-axis (or z-axis) is parallel to the interface and the x-axis is perpendicular to the interface and thus parallel (or antiparallel) to the applied electric field E, such that the R-mode observed in the ellipsometry spectra has y-polarization. In this case the renormalization of the k_{LX} stiffness constant for the Ω_R(y) R-mode is determined by the anharmonicity constant H and the induced polar moment P_x (S10). The lack of a clear effect on the R-mode in the experimental spectra under a positive voltage thus confirms that the constant H is rather small and thus can be neglected. For the constant G the sign is per se unknown but the pronounced redshift of the R-mode in the experimental data at negative voltage suggests that $G < 0$.

Note that the above described scenario is confirmed by the temperature dependence of the R-mode in zero electric field (without any static polar moment). Supplementary Figure 5 shows that the R-mode exhibits an anomalous softening toward low temperature that is accounted for by the corresponding enhancement of the AFE and FE fluctuations (see also [10]).

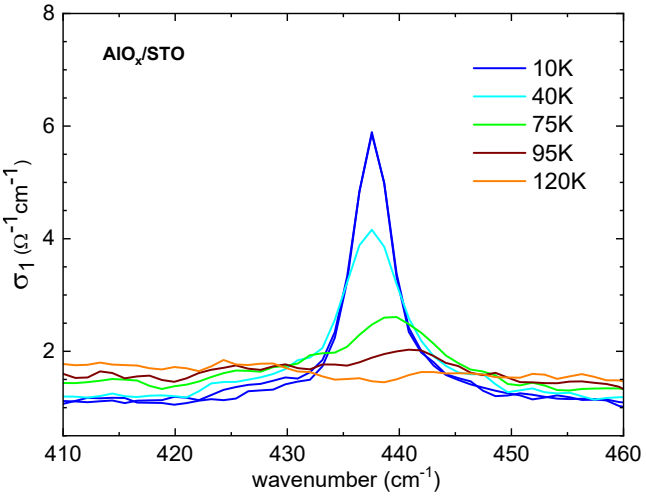

Supplementary Figure 5: Zero field R-mode behaviour as a function of temperature in STO-structures.

To summarize, the above considered stiffness softening mechanism and anharmonicity mechanism with $H<<G$ and $G<0$ are both contributing to the R-mode splitting in the polar phase with a static moment **P** for which the R-mode frequency exhibits a sizeable redshift for the component parallel to **P** whereas it is hardly affected for the ones perpendicular to **P**.

Finally, since in the main text of the paper we conjecture that the static polar moment is along a diagonal direction, we consider the case that $\mathbf{P_0}$ is at an oblique angle θ with respect to the z-axis (the tetragonal C_4-axis). Since the dynamic polar moments of the R-mode occur in the plane perpendicular to the C_4-axis (the z-axis) we make a new choice with the x' - axis along the projection of the static polar moment on the xy-plane. The antiferroelectric moment $L_{y'} \propto |\boldsymbol{P}_\theta|' \sin\theta$. The stiffness parameter in the new x'y' coordinate system thus have the form $\tilde{k}_{LY'} = k_{LS} + G\,|\boldsymbol{P}_\theta|^2 \sin^2\theta < k_{LX'} = k_L$ and $k_{PX'} = k_{PS}\sin\theta + k_P\cos\theta < k_{PY'} = k_P$ for which the redshift with Ω_R(x') < Ω_R(y') depends on the oblique angle θ and vanishes for θ=0.

Supplementary Note 5: Polar distortion and the R-mode splitting in infrared ellipsometry

Here we outline, that the R-mode splitting in the infrared ellipsometry data (see Fig. 1a-d of the manuscript) can only occur in the presence of a sizeable in-plane component of the polar distortion, $\mathbf{P_{ab}} > 0$, whereas the perpendicular component, $\mathbf{P_c}$, does not contribute to the R-mode splitting.

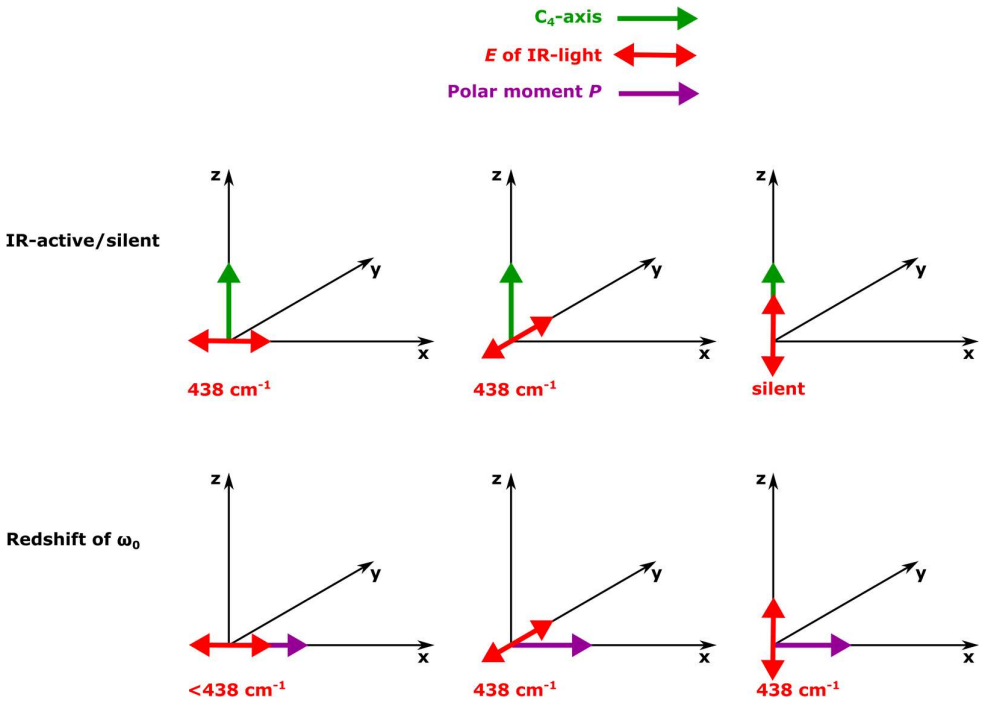

Supplementary Figure 6: Dependence of the frequency and IR-activity of the R-mode on the orientation of the electric field vector E (red) with respect to the C_4-axis (green) and the polar moment P (purple).

The frequency and the IR-activity of the R-mode depends on the orientation of the polarization, **P**, and the C_4-axis as follows (and sketched in Supplementary Figure 6):

1. The R-mode at 438 cm^{-1} is IR-active only in the tetragonal state below T^*=105 K and only if the light polarization vector, **E**, is perpendicular to the tetragonal C_4-axis (upper panel).

2. The redshift of the eigenfrequency ω_0 of the R-mode occurs only for the component of the vibration that is parallel to the polar distortion, **P**. The eigenfrequency ω_0 of the perpendicular components of the R-mode is not (or hardly) affected and remains at 438 cm^{-1} (bottom panel).

3. Despite the grazing angle of incidence of φ = 75 degrees, the infrared ellipsometry response in the vicinity of the R-mode (i.e. well away from the LO_4 edge) is governed by the in-plane component of the dielectric function, see also Supplementary Note 2.

Consequently, there are three different possible scenarios:

Scenario I: *P* is parallel to the C_4-axis

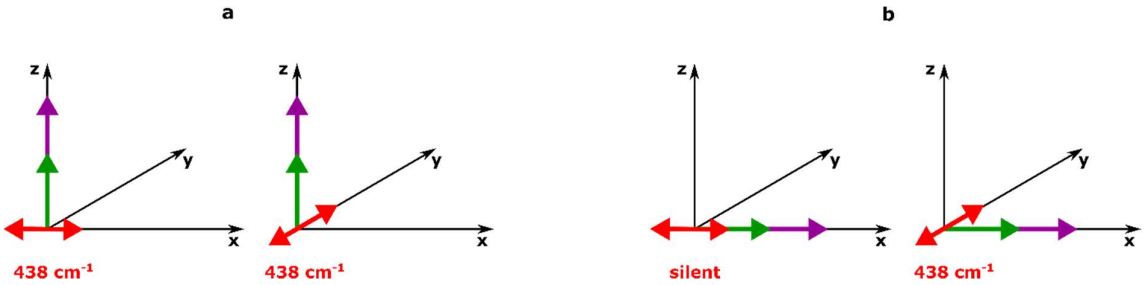

Supplementary Figure 7: Scenario I*. The polar moment* ***P*** *is parallel to the C_4-axis. Then,* ***P*** *and the C_4-axis can be either parallel (a) or perpendicular (b) to the z-axis of the crystal (or the surface normal). In both cases, no R-mode splitting can be seen.*

Scenario I (see Supplementary Figure 7) demonstrates that the R-mode splitting can only be seen, if **P** has a sizeable component perpendicular to the C_4-axis. This is the case in the following Scenario II and III.

Scenario II: *P* is perpendicular to the C_4-axis

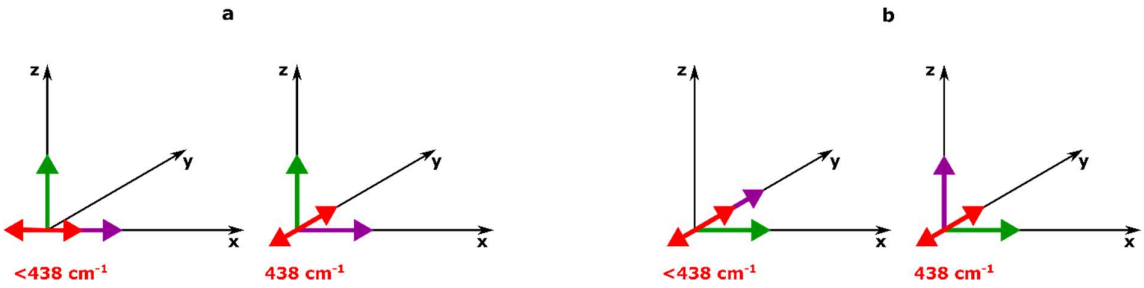

Supplementary Figure 8: Scenario II*. The polar moment* ***P*** *is perpendicular to the C_4-axis, which can be oriented out-of-plane (a) or in-plane (b). A softening of the R-mode can be observed only for the in-plane component of the polar moment* $\boldsymbol{P}_{ab}$*, whereas for the perpendicular component* $\boldsymbol{P}_c$ *it remains constant. The R-mode splitting occurs when both kinds of domains are present in the sample.*

Scenario III: *P* is along the diagonal direction

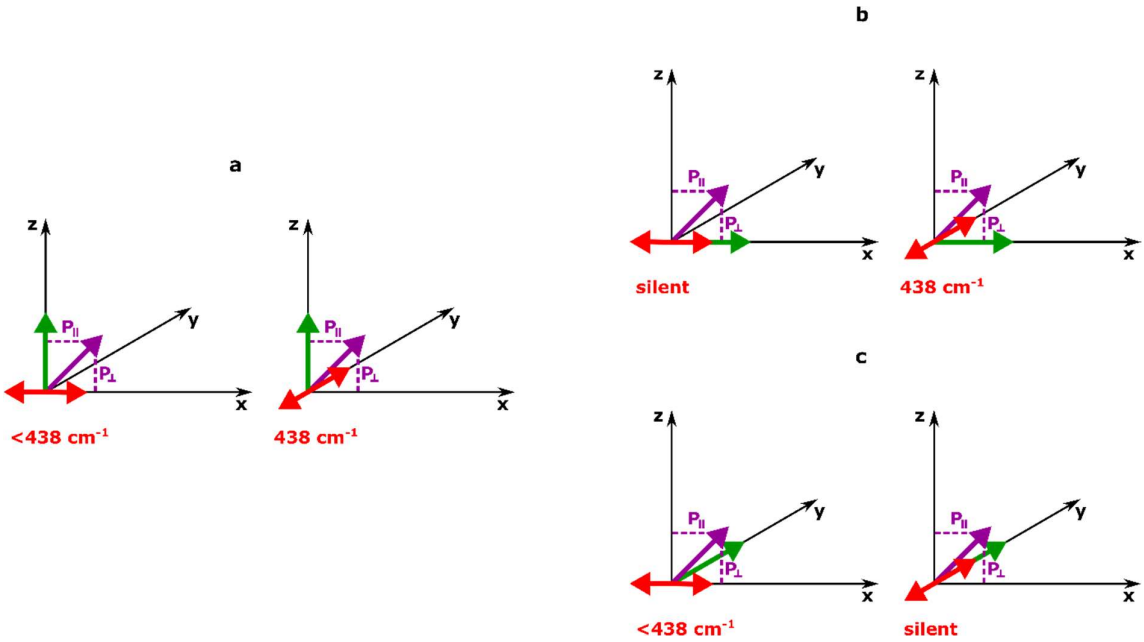

Supplementary Figure 9: Scenario III*. The polar moment* ***P*** *is along a diagonal crystallographic direction, where the C4-axis is parallel (a) or perpendicular (b,c) to the z-axis. In all cases, a splitting of the R-mode occurs. Note that in (b,c), the R-mode splitting occurs via a mixture of domains.*

As a result, in both the Scenario II (Supplementary Figure 8) and the Scenario III (Supplementary Figure 9), the R-mode splitting occurs due to the in-plane component of **P**!

Supplementary Note 6: Fitting of the gate-voltage-induced LO_4 edge anomaly

The dielectric function of $SrTiO_3$ is governed by infrared-active phonons and has been described as a sum of Lorentz oscillators:

$$\varepsilon(\omega) = \varepsilon_\infty + \sum_{j=1}^{K} \frac{S_j}{\omega_j^2 - \omega^2 - i\omega\gamma_j} \qquad \text{(S13)}$$

Note that the contribution from the 2DEG is small and therefore neglected in the model. The parameters of the Lorentz oscillators are the oscillator strength S_j, the eigenfrequency ω_j, and the broadening γ_j. For the TO_1 soft mode, in addition, an asymmetry factor σ=0.008 has been included to account for its rather strong anharmonicity [1]. A high frequency dielectric constant of ε_∞=5.88 was used to account for the contribution of the high energy excitations (inter-band transitions) which remains frequency independent in the infrared regime.

In order to properly fit the new TO mode which arises close to the LO_4 edge when applying a negative back-gate voltage on the sample (-V), it is necessary to use an anisotropic model (since the only component becoming IR-active is the one parallel to the induced polar moment, **P**).

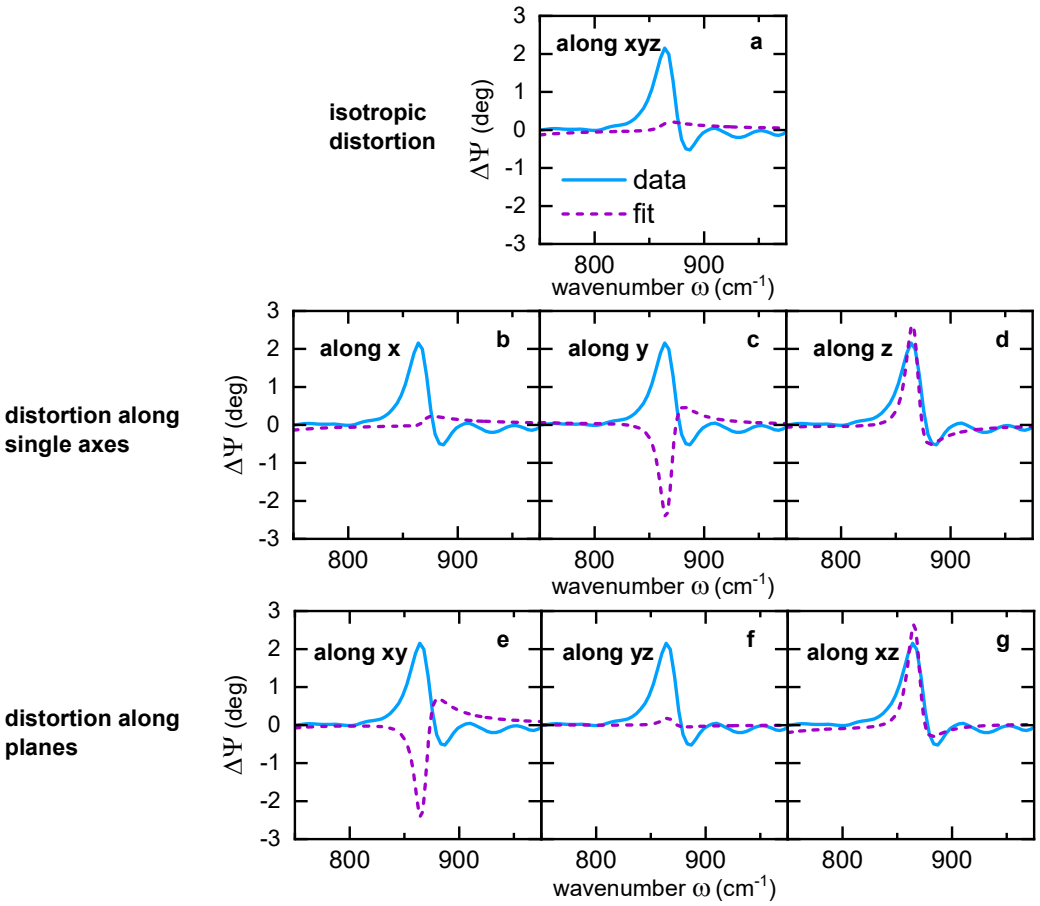

Supplementary Figure 10: Fitting of the gate-voltage-induced LO_4 edge anomaly. *Shown are the difference plots of $\Delta\Psi=\Psi_{-5kV/cm} - \Psi_{0V,\ pristine}$ in the vicinity of the LO_4 edge of LAO/STO at 40 K, for several model scenarios. In all graphs, the parameters of the new TO mode were set to $S_{newTO} = 3329.3\ cm^{-2}$, $\omega_{newTO} = 710\ cm^{-1}$, $\gamma_{newTO} = 7\ 5\ cm^{-1}$. The data are shown by the solid cyan lines, the fits by the dashed purple lines.*

Supplementary Figure 10 shows a comparison of the fits for which **P** and thus the IR-active component of the TO-mode is assumed to have (a) equal x-, y- and z- components, (b) only a x-component , (c) only a y-component, (d) only a z-component, (e) equal x- and y- components, (f) equal y- and z- components, and (g) equal x- and z- components.
Note that the x-axis is defined by the cross-section of the sample surface with the plane of incidence of the photons, and y- and z- are the corresponding orthogonal axes that are parallel and perpendicular to the sample surface, respectively. It is evident from Supplementary Figure 10 that a reasonable fit of the LO_4 edge anomaly at -V can requires that the TO mode and thus **P** has a finite z-component.

The analysis of the corresponding R-mode splitting (see Fig. 1a-d in the manuscript) reveals that **P** has also a sizeable in-plane component. The combined behavior of the LO_4 edge anomaly and the R-mode splitting thus suggests that **P** has comparable in-plane and out-of-plane components and is likely pointing along one of the diagonals with respect to the Ti-O bonds (or the x-, y- and z-axes). Moreover, the orientation of the diagonal polarization may vary along the lateral directions (between ±xz and ±yz).

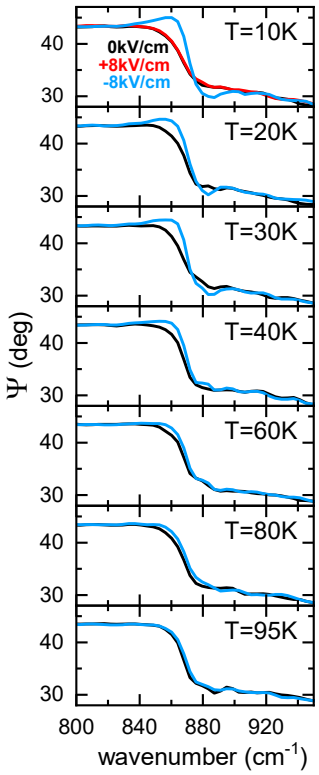

Supplementary Figure 11: Temperature dependence of the gate-voltage induced LO_4 edge anomaly of AlO_x/STO. *The spectra are shown in terms of the ellipsometric angle Ψ.*

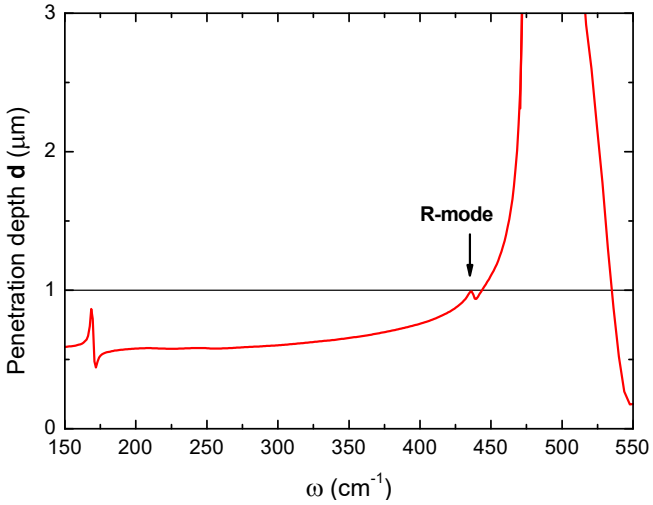

Supplementary Figure 12: Resolution of the infrared ellipsometry technique. *Penetration depth* ***d*** *of the infrared light in bare $SrTiO_3$ at low temperature, as obtained from the measured dielectric function with* $\boldsymbol{d} = \frac{\lambda}{4\pi * k(\omega)}$*, with the wavelength λ and the extinction coefficient, k. Here,* ***d*** *is defined as the depth inside the sample, where the lights intensity is dropped down to 1/e of its original value. Around the R-mode at 438 cm^{-1} (black arrow) the light penetrates less than ~1 μm inside the sample. Near the LO_4 edge at ~800 cm^{-1}, the material's refractive index is smaller than the one of the ambient, which leads to total reflection: The light becomes an evanescent wave, and therefore penetrates also just <1 μm.*

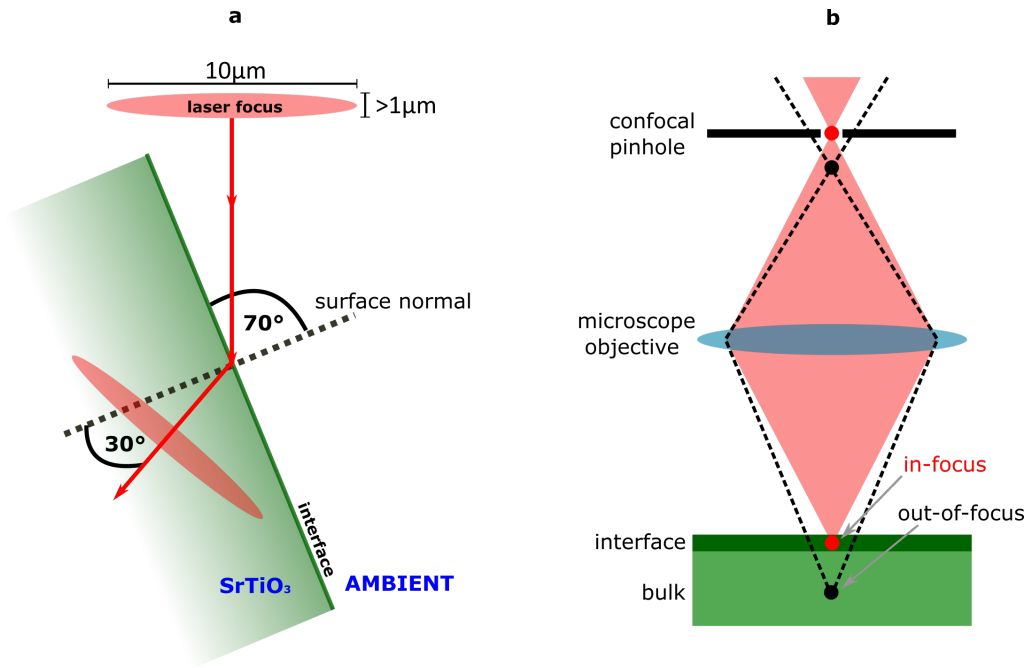

Supplementary Figure 13: Depth resolution of the confocal Raman spectroscopy technique. *(a) Schematic showing an estimate of the depth resolution of the confocal Raman experiment with a wedged sample holder for which the incident laser beam in the ambient (inside the sample) is at 70 degrees (~30 degrees) with respect to the surface normal. Indicated with a red ellipse is the horizontal and vertical resolution that is defined by the focusing components (i.e. lenses etc.). With a ×100 long working distance objective lens and a short depth of focus, NA=0.6, the horizontal resolution is estimated to be ≲ 10 µm. The estimate of the vertical resolution is more complex, but certainly larger than 1 µm. (b) Principle of confocal Raman spectroscopy (adapted from the supplementary information of [11]). The confocal hole suppresses residual scattered light from out-of-focus points.*

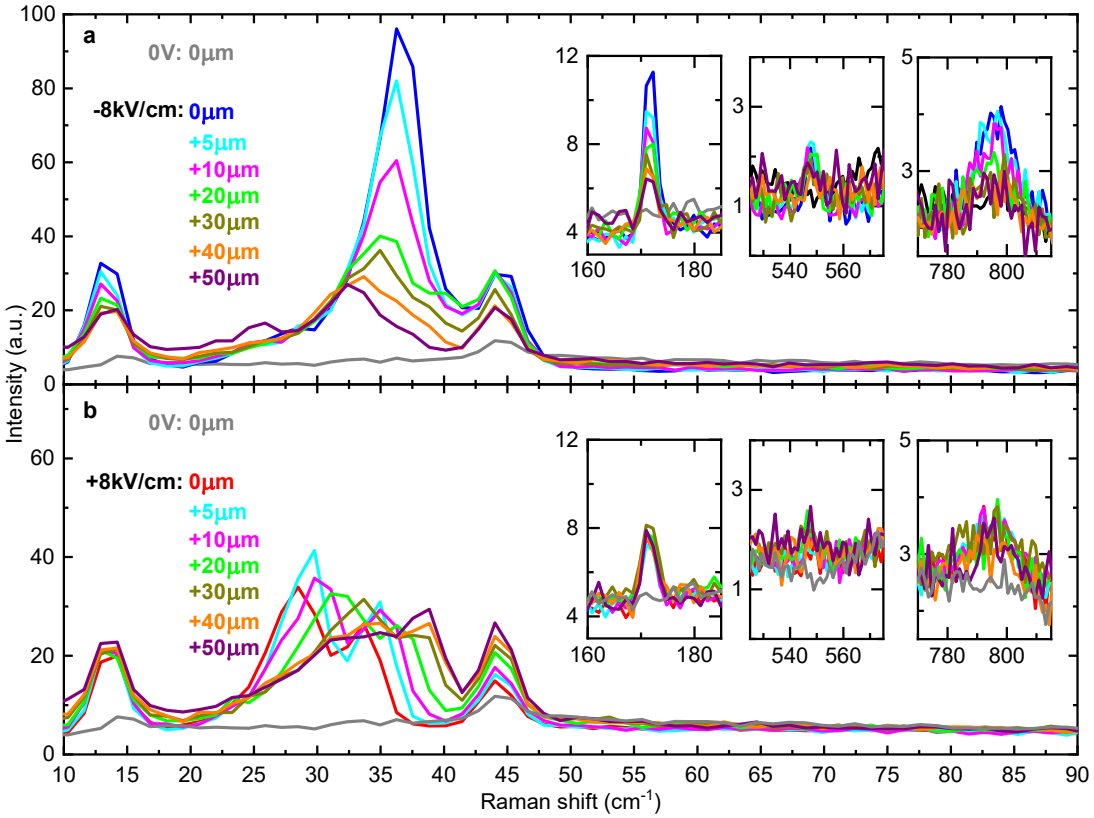

Supplementary Figure 14: Depth profiling confocal Raman spectra. *The spectra of AlO_x/STO were taken for different depths in micrometer steps at T≈ 30 K in p-polarization at -8 kV/cm (a) and +8 kV/cm (b). Insets show the corresponding depth evolution of the other electric-field induced infrared-active modes. The spectra are normalized to the multi-phonon background, and to the R-mode at 144 cm^{-1}.*

Supplementary Note 7: Temperature determination via Bose-Einstein relation

In Raman experiments, the real sample temperature can be higher than the value shown by an inserted sensor diode inside the cryostat, due to laser heating. For our setup settings, we can estimate the laser power arriving to the sample to be < 1 mW (see supplementary information of [11]). As described above, we obtain a maximal temperature offset of ≲ 20 K by comparing the Stokes to the Anti-Stokes signal.

Via the Bose-Einstein distribution, it is possible to compare the probability of Stokes- with Anti-Stokes scattering (in the classical picture it is the Boltzmann distribution) such as

$$\frac{I_{AS}}{I_S} \sim e^{-\frac{h \cdot v_R}{k_B T}} \tag{S14}$$

As displayed in Supplementary Figure 15, this relation can be used to accurately determine the sample's temperature [12], [13], as

$$T_{sample} = (h \cdot v_R) / \left[k_B \cdot \left(\log\left(\frac{I_S}{I_{AS}}\right) + 3 \cdot \log\left(\frac{v_0 + v_R}{v_0 - v_R}\right) \right) \right] \tag{S15}$$

with the Planck constant h=6.626 × 10^{-34} [Joule × second], the Boltzmann constant k_B=1.38 × 10^{-23} [Joule/Kelvin], v_0 the energy of the laser light and v_R being the Raman shift of the field induced TO_1 mode (in our case). I_S (I_{AS}) is the peak area of the TO_1 mode on the Stokes (Anti-Stokes) side, subtracted with the peak area of the spectra of 0 V (with no TO_1 mode).

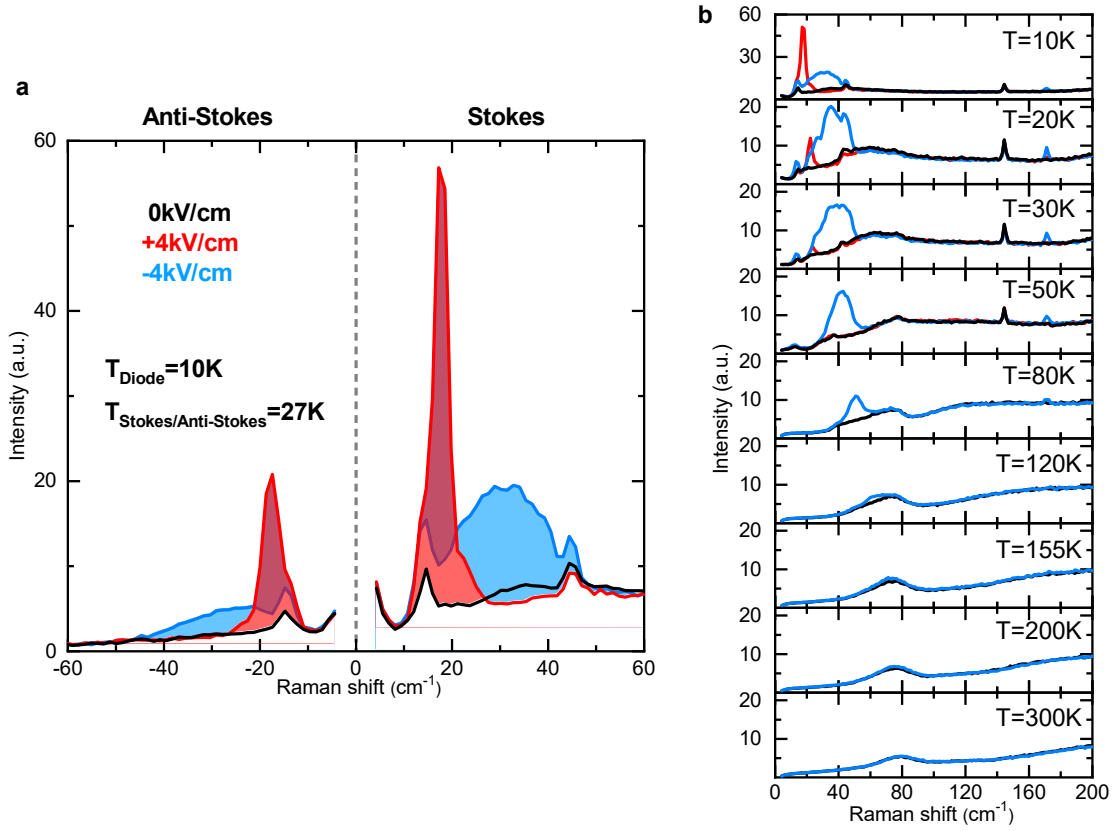

Supplementary Figure 15: Estimate of the laser heating effect and the temperature evolution of the soft-mode intensity at ±4 kV/cm in the confocal Raman spectra of LAO/STO. *(a) Estimate of the sample temperature at the laser spot at the base temperature of the He-flow cryostat of 10 K, obtained from an analysis of the peak area of the induced soft mode on the Stokes to the Anti-Stokes side, via the Bose-Einstein distribution. It shows that the maximal temperature offset, as compared to the one measured by the diode (which was mounted close to the sample inside the cryostat) is less than 20 K. Note that the strongest laser heating occurs at base temperature, this offset thus will be reduced at higher temperatures. (b) Temperature dependence (with respect to the diode value) of the Bose-factor corrected spectra.*

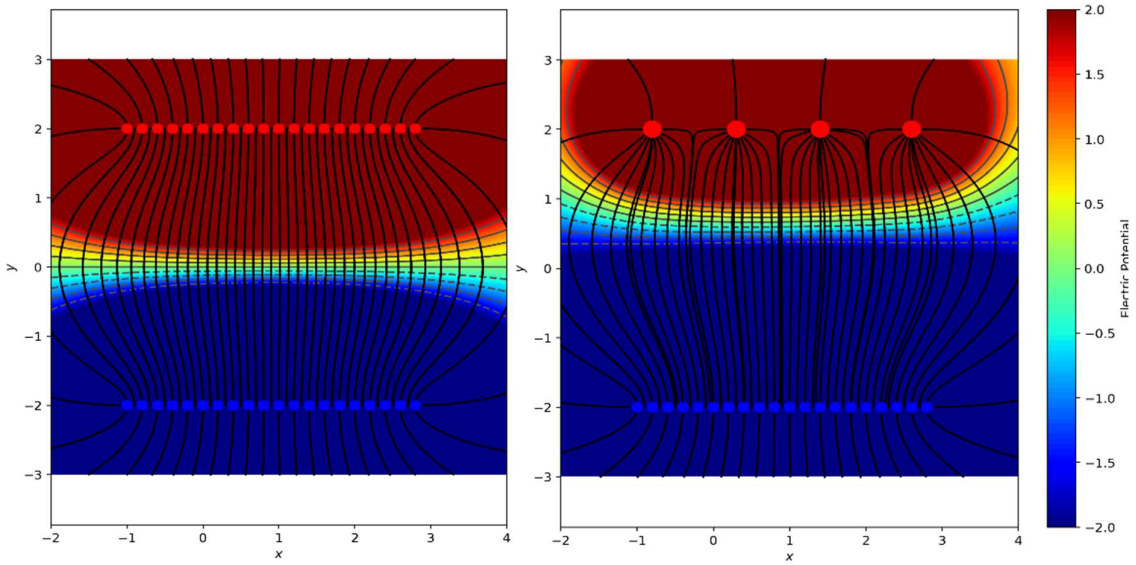

Supplementary Figure 16: Simulation of electric field lines. *The simulated electric field for a homogeneous top-electrode is shown in the left panel in which the positive back-gate induces a usual capacitor. The right panel shows an inhomogeneous top-electrode for the case of negative back-gate, where the surface electrode is depleted and leads to in-plane electric field lines (black color).*

Supplementary Note 8: Additional macro (non-confocal) Raman measurements

Additional Raman macroscopic measurements as a function of gate-voltage were performed at the Laboratoire Matériaux et Phénomènes Quantiques (LMPQ) in Université de Paris, with a triple spectrometer Jobin Yvon T64000. A comparable AlO_x/STO sample was prior measurements thinned down to 250±20 µm by mechanical polishing on diamond pads under deionized water flow. Incident and scattered beam are focused and collected through lenses, respectively. The excited volume is roughly given by the focus (~70 µm), i.e. around one order of magnitude larger than with the confocal Raman setup. Therefore, the measured macro-Raman spectra contain an average of all contributions and several domains, but are mostly sensitive to the bulk component. The excitation beam corresponds to the 514 nm laser line with a power of ca. 0.1 mW to minimize laser heating. The laser light is focused on the sample at an angle of 35-40 degrees to the surface normal. The temperature is controlled with an open cycle Helium cryostat.

Supplementary Figure 17 shows the AlO_x/STO Raman spectra measured at 15 K and low frequency with positive and negative gate-voltages of ±3 and ±6 kV/cm. The peaks at 15 cm^{-1} and 45 cm^{-1} are associated to the E_g and A_{1g} phonon modes, respectively. This mode characterized the transition is triply degenerated in the cubic phase and is inactive in Raman. This mode becomes Raman-active and splits into two modes E_g = 15 cm^{-1} and A_{1g} = 45 cm^{-1} in the tetragonal phase below T^*=105 K. The orientation of the sample with respect to the incident beam allows to probe the out-of-plane polar moment, $\mathbf{P}_c$, to some extent, but less than with the micro-Raman configuration. The asymmetry with the sign of the gate-voltage observed in confocal micro Raman and associated with a surface effect can still be observed at the macroscopic scale. The observed phenomenon takes place on the first 20 µm of the sample, which represents about 1/3 of the probed depth in macroscopic configuration.

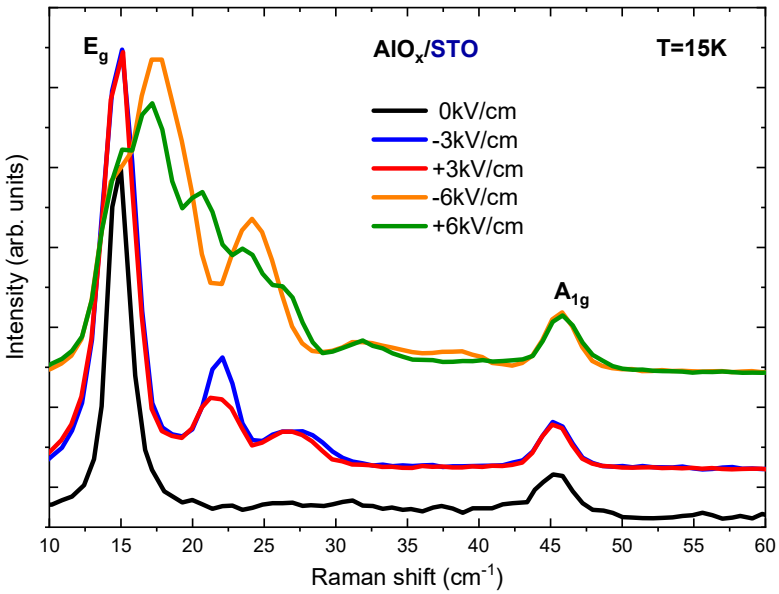

Supplementary Figure 17: Macro Raman spectra. *The spectra show the Raman response a the macroscopic scale of $AlO_x/SrTiO_3$ as a function of gate-voltage at 15 K. The E_g and A_{1g} phonon modes at 15 and 45 cm^{-1} become Raman-active below T*=105 K. Both modes are not modified by the gate-voltage. Low-frequency Raman spectra show an asymmetric behavior depending of the gate-voltage sign.*

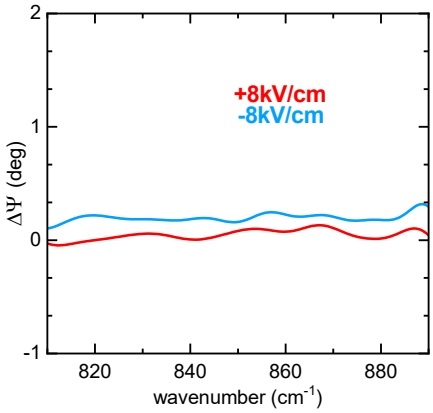

***Supplementary Figure 18*: Infrared response of back-gated $AlO_x/KTaO_3$ at 10 K.** *Since $KTaO_3$ remains cubic down to low temperatures, there is no infrared-active R-mode (around 438 cm^{-1}) that can be used to study to anomalous polarization behavior. Nevertheless, the corresponding anomaly at the LO_4 edge, as shown in Fig. 1e of the manuscript for the case of LAO/STO, should still occur in response an induced anomalous polarization at -8 kV/cm. Supplementary Figure 18 shows that this is not the case, i.e. that a corresponding polarization does not develop in the vicinity of the AlO_x/KTO interface.*

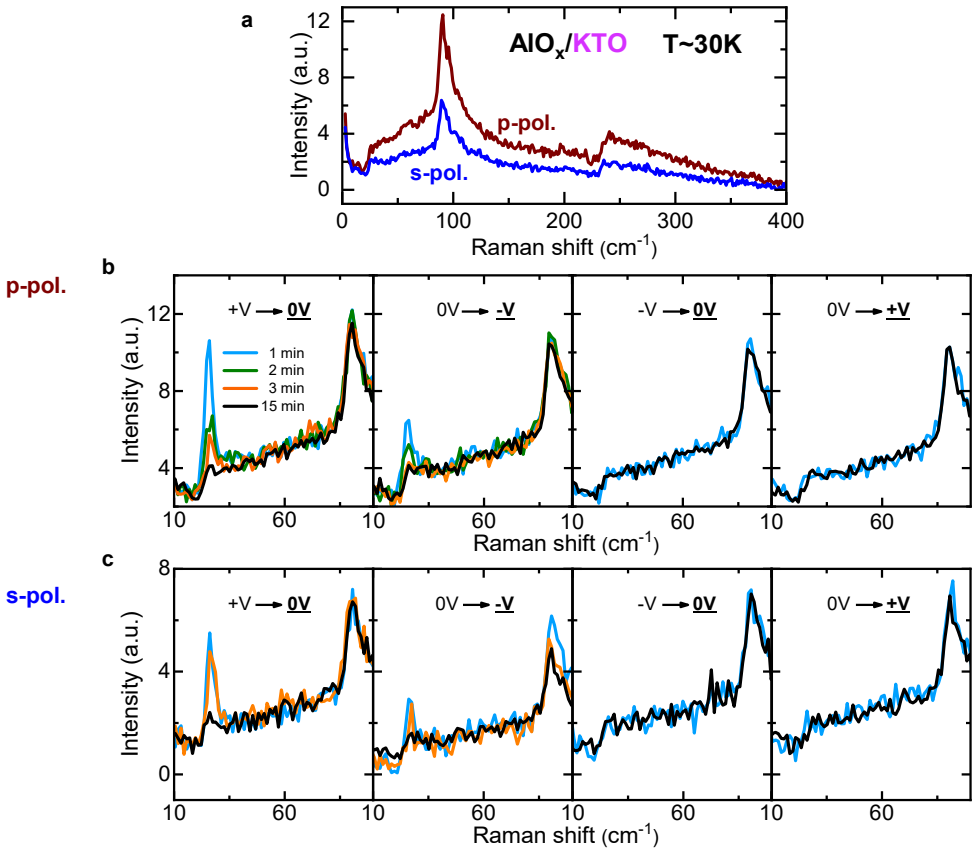

Supplementary Figure 19: Confocal Raman spectra of back-gated $AlO_x/KTaO_3$ measured in grazing-incidence, with +-8 kV/cm. *(a) Zero voltage spectra for different polarization geometries. Note that the detector is more efficient for the dark red curve (p-polarization) than for the blue one (s-polarization). The induced soft mode occurs only after the voltage has been decreased (from +V → 0V or from 0V → -V) but not after a corresponding increase of V. The amplitudes of the induced soft modes for p-pol. (b) and for s-pol. (c) are comparable. The induced soft mode occurs only below ~30 K and has only a weak depth dependence.*

Supplementary References

[1] M. Rössle "Infrared ellipsometry study of the lattice and charge dynamics in bulk $SrTiO_3$, thin $SrTiO_3$ films, and $LaAlO_3/SrTiO_3$ heterostructures" PhD thesis (2012)

[2] J. Petzelt, T. Ostapchuk, I. Gregora, I. Rychetský, S. Hoffmann-Eifert, A. V. Pronin, Y. Yuzyuk, B. P. Gorshunov, S. Kamba, V. Bovtun, J. Pokorný, M. Savinov, V. Porokhonskyy, D. Rafaja, P. Vaněk, A. Almeida, M. R. Chaves, A. A. Volkov, M. Dressel and R. Waser "Dielectric, infrared, and Raman response of undoped $SrTiO_3$ ceramics: Evidence of polar grain boundaries" *Phys. Rev. B,* vol. 64, no. 18, p. 184111, 10 (2001)

[3] H. Fujiwara "Spectroscopic Ellipsometry: Principles and Applications" *John Wiley & Sons* (2003)

[4] M. Schubert "Infrared Ellipsometry on Semiconductor Layer Structures " Springer (2004)

[5] C. Bernhard, J. Humlícek and B. Keimer "Far-infrared ellipsometry using a synchrotron light source—the dielectric response of the cuprate high-T_c superconductors" *Thin Solid Films,* Vols. 455-456, pp. 143-149 (2004)

[6] N. Sai and D. Vanderbilt "First-principles study of ferroelectric and antiferrodistortive instabilities in tetragonal $SrTiO_3$" *Phys. Rev. B,* vol. 62, no. 21, pp. 13942-13950, 12 (2000)

[7] J. Hemberger, P. Lunkenheimer, R. Viana, R. Böhmer and A. Loidl "Electric-field-dependent dielectric constant and nonlinear susceptibility in $SrTiO_3$" *Phys. Rev. B,* vol. 52, no. 18, pp. 13159-13162, 11 (1995)

[8] H. Vogt "Refined treatment of the model of linearly coupled anharmonic oscillators and its application to the temperature dependence of the zone-center soft-mode frequencies of $KTaO_3$ and $SrTiO_3$" *Phys. Rev. B,* vol. 51, no. 13, pp. 8046-8059, 4 (1995)

[9] P. A. Fleury and J. M. Worlock "Electric-Field-Induced Raman Scattering in $SrTiO_3$ and $KTaO_3$" *Phys. Rev.,* vol. 174, no. 2, pp. 613-623, 10 (1968)

[10] M. Rössle, K. W. Kim, A. Dubroka, P. Marsik, C. N. Wang, R. Jany, C. Richter, J. Mannhart, C. W. Schneider, A. Frano, P. Wochner, Y. Lu, B. Keimer, D. K. Shukla, J. Strempfer and C. Bernhard "Electric-Field-Induced Polar Order and Localization of the Confined Electrons in $LaAlO_3/SrTiO_3$ Heterostructures" *Phys. Rev. Lett.,* vol. 110, no. 13, p. 136805, 3 (2013)

[11] M. Hepting, M. Minola, A. Frano, G. Cristiani, G. Logvenov, E. Schierle, M. Wu, M. Bluschke, E. Weschke, H.-U. Habermeier, E. Benckiser, M. Le Tacon and B. Keimer "Tunable Charge and Spin Order in $PrNiO_3$ Thin Films and Superlattices" *Phys. Rev. Lett.,* vol. 113, no. 22, p. 227206, 11 (2014)

[12] I. P. Herman "Peak temperatures from Raman Stokes/anti-Stokes ratios during laser heating by a Gaussian beam" *J. Appl. Phys.,* vol. 109, p. 016103 (2011)

[13] K. Fürsich, J. Bertinshaw, P. Butler, M. Krautloher, M. Minola and B. Keimer, "Raman scattering from current-stabilized nonequilibrium phases in Ca_2RuO_4," *Phys. Rev. B,* vol. 100, no. 8, p. 081101, 8 (2019)